# GPU-based 3D iceball modelling for fast cryoablation simulation and planning

## IJCARS / MICCAI 2018 invited paper

Ehsan Golkar · Pramod P. Rao · Leo Joskowicz · Afshin Gangi · Caroline Essert

**Abstract** *Purpose* The elimination of abdominal tumors by percutaneous cryoablation has been shown to be an effective and less invasive alternative to open surgery. Cryoablation destroys malignant cells by freezing them with one or more cryoprobes inserted into the tumor through the skin. Alternating cycles of freezing and thawing produce an enveloping iceball that causes the tumor necrosis. Planning such a procedure is difficult and time-consuming, as it is necessary to plan the number and cryoprobe locations, and predict the iceball shape which is also influenced by the presence of heating sources, e.g., major blood vessels and warm saline solution injected to protect surrounding structures from the cold.

*Methods* This paper describes a method for fast GPU-based iceball modeling based on the simulation of thermal propagation in the tissue. Our algorithm solves the heat equation within a cube around the cryoprobes tips and accounts for the presence of heating sources around the iceball.

*Results* Experimental results of two studies have been obtained: an ex-vivo warm gel setup, and simulation on five retrospective patient cases of kidney tumors cryoablation with various levels of complexity of the vascular structure and warm saline solution around the tumor tissue. The experiments have been conducted in various conditions of cube size and algorithm implementations. Results show that it is possible to obtain an accurate result within seconds.

*Conclusion* The promising results indicate that our method yields accurate iceball shape predictions in a short time and is suitable for surgical planning.

Ehsan Golkar
ICube, Université de Strasbourg, France
Medical Image and Signal Processing Research Center, Isfahan University of Medical Sciences, Isfahan, Iran

Caroline Essert
ICube, Université de Strasbourg, France
E-mail: essert@unistra.fr

Pramod P. Rao and Afshin Gangi
Department of Radiology, University Hospital of Strasbourg, France

Leo Joskowicz
School of Computer Science and Engineering, The Hebrew Univ. of Jerusalem, Israel

## 1 Introduction

The treatment of abdominal tumors has undergone significant improvements with the introduction of percutaneous procedures based on thermal ablation. The advantages of these minimally invasive procedures is that they lead to faster patient recovery, shorter hospital stays, lower patient morbidity, and fewer, smaller skin scars. Oftentimes, they also preclude total organ removal, preserve most of the treated organ functionality, and enable the treatment of patients that cannot undergo open surgery or organ resection.

Cryoablation is a percutaneous procedure that was first introduced in the 1960s [1, 2]. Cryoablation interventions destroy malignant tumor cells by freezing them with one or more needles, called cryoprobes, inserted into the tumor through the skin under imaging guidance, e.g., CT, MR or ultrasound. Alternating cycles of freezing and thawing by decompressing a gas through the cryoprobes tips produce an enveloping iceball that causes the tumor necrosis [3]. The recommended temperature to achieve destruction of cancerous cells is -50°C to 0°C [4].

The numerous advantages of percutaneous cryoablation have made this procedure very popular in the past two decades [5]. However, the difficulties of planning an optimal position for the cryoprobes and of anticipating the final result is a limitation in many cases [6–8]. Indeed, to be most effective, cryoablation requires careful preoperative planning of the cryoprobes to be inserted. The goal is to find the number and positions for the cryoprobes that are safe and that produce an optimal iceball shape that covers the entire tumor with an additional margin to ensure its complete ablation. The simulation of the iceball formation and its final shape is required to ensure an effective treatment. However, simulating the iceball generated from multiple cryoprobes while taking into account various factors, i.e., the surrounding anatomy and the injection of protective warm fluid is challenging. Studies report success rates of 96% [9], with other cases being tumor recurrence or complications such as hemorrhage. In addition, the synergistic effect created by several cryoprobes depends on their actual location and influences the final shape of the iceball [10].

This paper describes in more detail a new method presented at MICCAI 2018 [11]. The approach is a fast and accurate GPU-based modeling of the iceball based on the simulation of thermal propagation in tissue based on the solution of the heat equation that accounts for the influence of heating sources around the iceball. The paper is organized as follows. We start with a brief review of the relevant state of the art. Next, we describe a fast GPU-based method for simulating the cold propagation in tissue from the freezing cryoprobe tips and for modeling the resulting iceball. We then present two experiments that validate our model: an ex-vivo setup with warm gel and five retrospective patient cases of kidney tumors cryoablation.

## 2 State of the Art

The accurate prediction of the iceball growth and final shape is essential to help the clinician to ensure the maximal coverage of the tumor while preventing possible damages to surrounding structures, and to choose the best insertion trajectories for the cryoprobes that will create the desired tumor-enclosing iceball.

Various research groups have proposed methods for computing the iceball shape to assist clinicians in preoperative planning. Butz *et al.* [12] developed one of the first simulations of a cryoablation iceball. In this early work, the iceball is modeled as a 3D ellipsoid forming around the cryoprobe tip without taking into account its surroundings. The iceball model is used in conjunction with a single cryoprobe placement optimization algorithm. Recent works describe advanced mathematical models to accurately simulate the growth and the final shape and size of the iceball in a simple, homogeneous gel surrounding, and in realistic soft tissue conditions. Most of these works base their models on the Pennes heat propagation equation [13]. However, the complexity, numerical sensitivity, and computational cost of this model motivated researchers to develop simplified models, which introduce unknown inaccuracies. Deng *et al.* [6, 14] describe a simplified model for multiple cryoprobes planning that simulates the iceball growth in an aquasonic clear ultrasonic gel. The shape of the iceball resulting from various cryoprobes is investigated in a laboratory environment. Ge *et al.* [15] incorporate surrounding gel models into the simulation but do not validate their results with real soft tissue properties. In subsequent papers [16, 17], the authors describe a model that accounts for the presence of vascular systems during freezing. Nabaei *et al.* [18] investigate the effect of blood vessels adjacent to tumors. Their theoretical study shows that large blood vessels (>4mm diameter) significantly affect the shape of the iceball, as the blood flow heat prevents the cold from propagating. Other studies describe advanced models validated in gel [19], or tailored to other organs, e.g., the prostate [8] and the lungs [20, 21].

None of the works discussed above focuses on the iceball simulation computation time, which can limit the scope of the preoperative planning by reducing to a handful the scenarios that can be simulated and tested. Indeed, the optimization of cryoprobes placement requires to iterate over many possible candidate cryoprobe configurations and to simulate the iceball at each iteration. Thus, the reduction of the computation time becomes important. In a recent study, Keelan *et al.* [22] focused on cryosurgery simulation and the implementation on graphic processing units. Their results showed computation times of about 200 s. with CPU, while an implementation using 512 GPU cores could decrease computation time to 2 seconds. In another study, Talbot *et al.* [7] describe a GPU-based method to compute the iceball resulting from multiple cryoprobes. Their method significantly decreases the iceball modelling computation time to <30 secs, but does not take into account the surrounding structures.

An alternative to cryoablation is hyperthermia, in which tumor necrosis is induced by extreme heat propagation instead of cold. The most common hyperthermia procedure is radio frequency ablation (RFA). As for cryoablation, several groups have investigated the modelling of the isothermal surface to predict the outcome and to evaluate the damages to adjacent structures.

Similarly to cryoablation surgery, the presence of adjacent cooling structures close to tumor and the acceleration of computation times are two major challenges

of RFA simulation. Villard *et al.* [23, 24] described a simplified ellipsoidal model that takes into account nearby vascular structures. The influence of blood vessels near the tumor was also investigated more recently in [25]. Advanced models for RFA have also been described in [26, 27]. None of these works attempts to reduce the simulation computation time. Rieder *et al.* [28] describe a GPU-based implementation of heat propagation for RFA procedures. Their model, which was developed for a single probe, is based on weighted distance fields, and has been simplified to allow real-time computation. In another study of multi-probe RFA simulation [29], computation time was accelerated up to 3 min using the GPU. All of works which described above use Finite Element Method (FEM) as a solution for bioheat equation while Lattice Boltzmann method (LBM) [30] and Finite Difference (FD) [31] were also suggested as an alternative solution to compute bioheat equation. The computational time of both methods can be massively high and GPU implementation is one of the options to overcome this limitation.

To the best of our knowledge, few studies have developed a fast implementation while using a realistic mathematical representation of heat propagation that accounts for the influence of surrounding anatomical structures, and have been evaluated on clinical cases. In this study, we propose a FEM solution of bioheat equation which is computationally efficient and validated in both gel and preoperative MR so it can be used with a probe placement optimization algorithm.

## 3 Materials and Methods

3.1 General formulation

The general formulation of heat equation describes the distribution of heat over time $t$ in a region defined in a Cartesian coordinate system [13]. The spatial propagation of heat in $(x, y, z)$ is described by the partial differential equation:

$$C\frac{\partial T}{\partial t} = \frac{\partial}{\partial x}(K_x \frac{\partial T}{\partial x}) + \frac{\partial}{\partial y}(K_y \frac{\partial T}{\partial y}) + \frac{\partial}{\partial x}(K_z \frac{\partial T}{\partial z}) + I(x, y, z, t) \qquad (1)$$

where $T$ is a temperature, $I$ is the internal heat generation function, $t$ is time, and constants $K$ and $C$ are the spatial thermal conductivities in $x, y, z$ and the heat capacity, respectively.

This continuous formulation can be approximated by a discretization in which $\Delta x = \Delta y = \Delta z$ is the spacing between a cell $(i, j, k)$ and its neighbours in the $x, y, z$ directions. The discrete formulation approximation is then:

$$T_{i,j,k}^{new} = T_{i,j,k} + \frac{\Delta t . \beta}{C_{i,j,k}(\Delta x)^3} . H_{i,j,k} \qquad (2)$$

where $C_{i,j,k}$ is the volumetric heat capacity. The new temperature $T_{i,j,k}^{new}$ after a time step $\Delta t$ is computed by adding to the previous temperature $T_{i,j,k}$ the heat flow coefficient $H_{i,j,k}$ multiplied by a relaxation factor $\beta \in [1, 2]$ (in our simulations, $\beta$ was set to 1.95).

In this formulation, the volumetric heat capacity $C_{i,j,k}$ at cell $(i, j, k)$ depends on the current temperature and is defined as:

$$C_{i,j,k} = \begin{cases} c_f & T_{i,j,k} < T_{ml} \\ \frac{q_l}{T_{mu}-T_{ml}} + \frac{c_f+c_u}{2}, & T_{ml} \le T_{i,j,k} \le T_{mu} \\ c_u & T_{i,j,k} > T_{mu} \end{cases} \tag{3}$$

where $c_f$ and $c_u$ represent the effective thermal capacities of frozen and unfrozen tissue, respectively, $q_l$ is the latent heat when the phase transition occurs, and $T_{ml}$ and $T_{mu}$ are the lower and the upper limits of the phase transition.

The heat flow $H_{i,j,k}$ for cell $(i,j,k)$ is computed from its six neighbours:

$$\begin{aligned} H_{i,j,k} = \; & \kappa_{i-\frac{1}{2},j,k}.(T_{i-1,j,k} - T_{i,j,k}) + \kappa_{i+\frac{1}{2},j,k}.(T_{i+1,j,k} - T_{i,j,k}) + \\ & \kappa_{i,j-\frac{1}{2},k}.(T_{i,j-1,k} - T_{i,j,k}) + \kappa_{i,j+\frac{1}{2},k}.(T_{i,j+1,k} - T_{i,j,k}) + \\ & \kappa_{i,j,k-\frac{1}{2}}.(T_{i,j,k-1} - T_{i,j,k}) + \kappa_{i,j,k+\frac{1}{2}}.(T_{i,j,k+1} - T_{i,j,k}) \end{aligned} \tag{4}$$

In this equation, $\kappa_{i-\frac{1}{2},j,k}$, $\kappa_{i,j-\frac{1}{2},k}$, $\kappa_{i,j,k-\frac{1}{2}}$ denote the thermal conductances between cell $(i,j,k)$ and the previous adjacent cells in the $x,y,z$ directions, respectively. Similarly, $\kappa_{i+\frac{1}{2},j,k}$, $\kappa_{i,j+\frac{1}{2},k}$, $\kappa_{i,j,k+\frac{1}{2}}$ denote the conductances between cell $(i,j,k)$ and posterior adjacent cells, as in [32].
The thermal conductance $\kappa_{i,j,k+\frac{1}{2}}$ is defined as:

$$\kappa_{i,j,k+\frac{1}{2}} = \frac{\Delta x \Delta y}{\Delta z/(2K_{i,j,k}) + \Delta z/(2K_{i,j,k+1}) + R_{i,j,k+\frac{1}{2}}} \tag{5}$$

where $K_{i,j,k}$ and $K_{i,j,k+1}$ are the thermal conductivities of the current cell $(i,j,k)$ and its adjacent cell $(i,j,k+1)$. The five other $\kappa$ values in Eq. 4 are defined similarly. In Eq. 5, the first two terms of the denominator represent the thermal resistances of cell $(i,j,k)$ and cell $(i,j,k+1)$ respectively. The third term, denoted $R_{i,j,k+\frac{1}{2}}$, is optional [32], and represents the thermal resistance at the interface between the two adjacent cells. Since the cells contain tissue with similar properties, this term has no impact on heating flows and is neglected in the rest of the paper.

Moreover, in our case the cells being isotropic ($\Delta x = \Delta y = \Delta z$), Eq. 5 can finally be simplified:

$$\kappa_{i,j,k+\frac{1}{2}} = \frac{2}{1/K_{i,j,k} + 1/K_{i,j,k+1}} \tag{6}$$

The thermal conductivity $K_{i,j,k}$ of a cell $(i,j,k)$ is defined as:

$$K_{i,j,k} = \begin{cases} K_f & T_{i,j,k} < T_{ml} \\ \frac{K_f+K_u}{2}, & T_{ml} \le T_{i,j,k} \le T_{mu} \\ K_u & T_{i,j,k} > T_{mu} \end{cases} \tag{7}$$

where $K_f$ and $K_u$ are the effective thermal conductivities for frozen and unfrozen tissue, respectively.

To avoid numerical instability in the heat transform equation, the time step $\Delta t$ is set to 0.05 secs, which satisfies the stability criterion [32]:

$$\Delta t < \frac{C_{i,j,k}(\Delta x)^3}{\Sigma \kappa}, \forall i,j,k \tag{8}$$

where

$$\Sigma\kappa = \kappa_{i-\frac{1}{2},j,k} + \kappa_{i+\frac{1}{2},j,k} + \kappa_{i,j-\frac{1}{2},k} + \kappa_{i,j+\frac{1}{2},k} + \kappa_{i,j,k-\frac{1}{2}} + \kappa_{i,j,k+\frac{1}{2}} \tag{9}$$

To simulate the growth of the iceball using this formulation, the 3D heat propagation is computed iteratively within a cubic grid of voxels centered at the cryoprobe tip, or at the centroid of the tips when several cryoprobes are used. To obtain a high accuracy, a very fine grid can be used, but at the cost of efficiency. In this study, we use a grid resolution of $\Delta x = \Delta y = \Delta z = 1$ mm, which is smaller than the diameter of the thinnest cryoprobe used in the procedures (*IceRod* by Galil Medical, diameter 1.5 mm); this value proved to be an appropriate trade-off between accuracy and speed.

In the simulation cube, the voxels located in the active part of the cryoprobes are labeled as the source of cold – their temperature is kept constant during the freezing cycles at the freezing temperature. Similarly, during active thawing cycles, they are kept constant at the active thawing temperature. During passive thawing cycles, the temperature in these voxels is computed as for normal tissue. Boundary conditions are represented by the voxels at the boundaries of the cube, which are set to be to the temperature of the environment.

### 3.2 Propagation of cold in the human body near heating sources

In the human body, heat is generated by metabolism, mostly from blood perfusion and reactions within the tissue cells. This heat production interferes with the cold propagation coming from the cryoprobes and influences the final size and shape of the iceball. Due to this phenomenon, the iceball growth is slower in-vivo than ex-vivo. To take this into account in the simulation, we add the thermodynamic properties of the human body in the last term of Eq. 1, which represents the internal heat generation:

$$C\frac{\partial T}{\partial t} = \frac{\partial}{\partial x}(K_x\frac{\partial T}{\partial x}) + \frac{\partial}{\partial y}(K_y\frac{\partial T}{\partial y}) + \frac{\partial}{\partial x}(K_z\frac{\partial T}{\partial z}) + C_b.\omega_b(T).(T_a - T_t) + Q_m \tag{10}$$

where $C_b$ denotes the heat capacity of blood, $\omega_b$ is the blood perfusion rate, $T$ is the tissue temperature, $T_a$ is the arterial temperature, $T_t$ is the temperature at time $t$, and $Q_m$ is the metabolic heat rate of tissue.

The blood perfusion rate $\omega_b(T)$ depends on the current temperature and is defined as:

$$\omega_b(T) = \begin{cases} 0 & T_{i,j,k} \leq T_{mu} \\ \omega_b & T_{i,j,k} > T_{mu} \end{cases} \tag{11}$$

The discrete approximation of Eq. 10 is then:

$$T_{i,j,k}^{new} = T_{i,j,k} + \frac{\Delta t.\beta}{C_{i,j,k}(\Delta x)^3}.H_{i,j,k} + C_b.\omega_b(T_{i,j,k}).(T_a - T_{i,j,k}) + Q_m \tag{12}$$

Another important source of interference with the propagation of cold in the human body is the presence of a major blood vessel or of injected warm protective
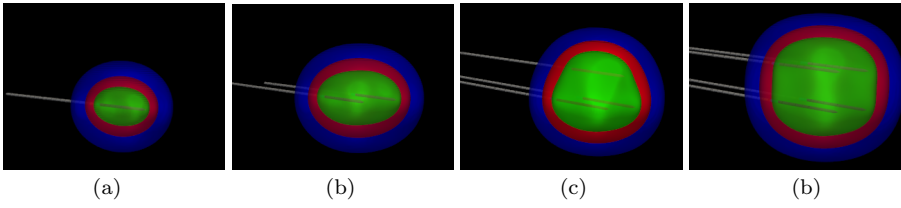
Fig. 1: In-silico validation. Iceball created at the end of simulation by one to four (a-d) evenly spaced cryoprobes (gray lines, left to right) arranged in parallel at 20mm intervals. The boundaries of the isothermal surfaces are shown for temperatures of 0°C (blue) -20°C (red) and -40°C (green).

liquid or gas close to the tumor and the iceball. The presence of these heat sources can significantly impair the normal propagation of cold and thus change the final shape of the iceball. To model this phenomenon, the voxels of the cube that corresponds to these structures are labeled, and their temperature is kept constant and equal to the source temperature during the entire simulation. In this paper, we assume that all sources of heat are constant and homogeneous.

### 3.3 Validation in-silico

We first validated the results of our model and simulation with an in-silico study using gel properties. The goal was to measure the performance of our simulation in terms of accuracy and computation times under theoretical conditions.

To achieve this goal, we ran various simulations using parameters that reproduced the conditions used in the physical experiment described in [33]. In that paper, the authors used a thermocouple matrix structure that was designed to measure the iceball temperatures in an ultrasound gel at 37°C. To simulate the same conditions, we used the thermophysical properties of a similar gel [34].

Since this experiment uses a gel, there is no internal heat generation. Thus, we use Eq. 1 and omit the last term, $I(x, y, z, t)$. Since the gel was maintained at a temperature of 37°C from the outside, the boundary conditions were applied with a fixed temperature of 37°C on the external voxels of the cube.

We simulated the propagation of cold with one to four evenly spaced cryoprobes arranged in parallel at 20mm intervals in a cube of $100 \times 100 \times 100$ mm$^3$. The configurations of cryoprobes is illustrated on Fig. 1 while the cube can be seen on Fig. 4. The experiment was conducted with the specifications of two types of cryoprobes from Galil Medical: *IceEdge* 2.4 mm (10G) and *IceRod* 1.5 mm (17G).

Each experiment simulated three cycles: 10 mins of freezing, followed by 5 mins of passive thaw, followed by 10 mins of freezing. We used the parameters provided by the manufacturer to model the action of the cryoprobes. For *IceEdge*, the freezing temperature at the cryoprobe's tip was set to $-138.0$°C, and the length of the active freezing part was set to 28mm starting at 5.2mm from the tip. For *IceRod*, the freezing temperature was set to $-119.4$°C, the length of the active freezing part was set to 31mm at 4.2mm from the tip.

For all settings, we computed the diameters of the resulting 0°C, -20°C and -40°C isotherm surfaces at their largest sections, perpendicularly to the probe's
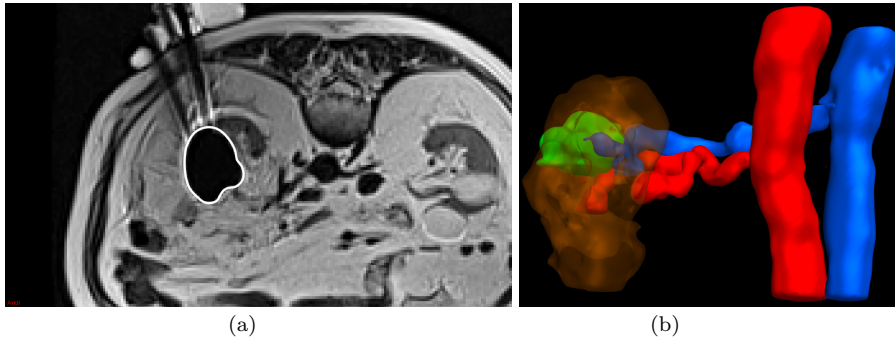
Fig. 2: Intraopertaive MRI scan validation. (a): representative MRI slice with the superimposed iceball contour (white); (b): visualization of the structures of interest after segmentation: kidney (brown), tumor (green), artery (red) and vein (blue).

axis. The isotherm surfaces are illustrated respectively in blue, red and green on Fig. 1. We then compared our simulation results with the dimensions measured in the physical world as reported in [33].

3.4 Validation on intraoperative MRI images

To validate our simulations in human body conditions, we conducted a second experiment using retrospective preoperative and intraoperative MRI scans of actual renal cryoablation procedures. Datasets of five patients were used, with different levels of complexity of the anatomical environment surrounding the tumor: tumor located close to major blood vessels, close to warm saline solution injected to protect sensitive organs nearby from being frozen, or far from heating structures.

The procedure performed by the surgeon differs from that of the gel experiment. The cryoablation process consisted of four cycles: 10 mins of active freezing, followed by 9 mins of passive thawing and 1 min of active thawing, and again 10 mins of active freezing. The active freezing temperature of *IceRod* was set to $-119.4^{\circ}$C; the active thawing temperature was set to $52.0^{\circ}$C. During the cryoablation, for some of the cases a saline solution at $37.0^{\circ}$C was continuously injected around the kidney.

The preoperative and intraoperative MRI scans of all patients have a resolution of $256 \times 232 \times 25$ voxels with a $1.5 \times 1.5 \times 5$ mm$^3$ voxel size. Images were acquired before cryoablation and at the end of the cryoablation process.

In the cases where a saline injection was performed between the preoperative and intraoperative images, the segmentation of the structures of interest was particularly challenging due to the deformation of the internal organs. Moreover, on the preoperative image the kidney and vessels are clearly visible, but there is no cryoprobe and no iceball. The intraoperative image contains the iceball and the cryoprobes, but the kidney is partly hidden by the iceball, deformed by saline solution, and the vessels are not always very easy to see. Therefore, we chose to register the preoperative images to the intraoperative images before the segmentation in order to be able to delineate all shapes in the same aligned space.

Table 1: Thermophysical properties of biological tissue and blood [15].

| Definition | Symbol | Unit | Value |
|---|---|---|---|
| Metabolic heat rate | $Q_m$ | $w.m^{-3}$ | 4200 |
| Latent heat | $q_l$ | $kJ.kg^{-3}$ | 2500 |
| Upper limit of phase transition | $T_{mu}$ | K | 272 |
| Lower limit of phase transition | $T_{ml}$ | K | 265 |
| Thermal conductivity of frozen tissue | $K_f$ | $W.m^{-1}.K^{-1}$ | 2.0 |
| Thermal conductivity of unfrozen tissue | $K_u$ | $W.m^{-1}.K^{-1}$ | 0.5 |
| Specific heat of frozen tissue | $c_f$ | $J.kg^{-1}.K^{-1}$ | 1800 |
| Specific heat of unfrozen tissue | $c_u$ | $J.kg^{-1}.K^{-1}$ | 3600 |
| Specific heat of blood | $c_b$ | $J.kg^{-1}.K^{-1}$ | 3850 |
| Blood perfusion rate per unit tissue volume | $\omega_b$ | $kg.m^{-3}.s^{-1}$ | 0.29 |

For each patient, we first registered the preoperative and the intraoperative MRI scan using interactive deformable point-based registration [35]. Then, on the registered preoperative MRI scan, we interactively segmented the kidney and the tumor using interactive segmentation. To obtain the ground-truth models of the structures of interest, we segmented on the intraoperative MRI scan the injected saline solution when it was present, the renal vessels (vein and artery) when they were close to the iceball, and the final iceball after the second freezing cycle. Note that during a cryoablation procedure, the iceball, which corresponds to the $0°C$ iso-surface, appears clearly as a black hole in the MRI scan (Fig. 2). We also segmented the cryoprobes, and used their positions as an input to reproduce the same setup in our simulations. Both the interactive segmentation and the registration were performed using MITK [35] and under the supervision of an experienced radiologist. Fig. 2 shows an example of a case.

The simulations were performed with commonly used soft tissue parameters accounting for frozen/unfrozen state [15], summarized in Table 1.

To measure the accuracy of our model and simulation, the Hausdorff distance and the Dice coefficient were computed to compare the similarity of the segmented and simulated iceball at the end of the process. This shape comparison was performed only for the $0°C$ iso-surface that corresponds to the iceball shape visible on the MRI image.

## 3.5 Parallelization

We implemented the method described above in three different setups. The first one is a simple, single-thread version. It consists of a sequential examination of the cube voxels to compute the new temperature at each voxel based on its previous state and those of its neighbours.

The second version is a multi-thread version that supports running in parallel several simulations. In this version, the cube is split into layers. The number of layers corresponds to the number of cores available on the computer CPU. The simulation within each layer can be run independently, as the currently computed temperatures only depend on the previous state but not on each other, so the different threads are not concurrent.

The third version has been implemented using the CUDA toolkit for NVidia's GPUs. To optimally use the parallelization capabilities of the GPU processing
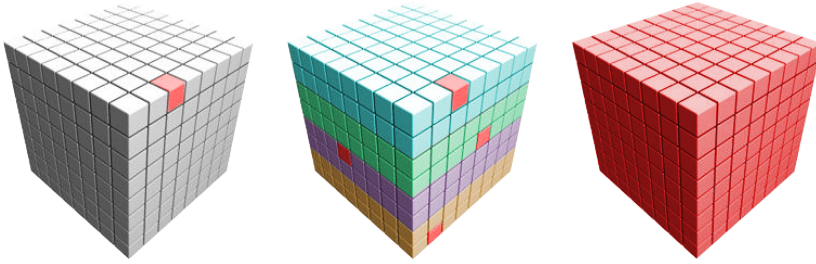
Fig. 3: Computation of the temperature at each voxel within the simulation cube with the different methods. Left: single thread version, one voxel (red) is computed at a time. Middle: multi-thread version, one voxel (red) per layer (blue, green, purple, yellow) are computed at the same time. Right: GPU version, a large number of voxels are computed at the same time.

units, we linearize the matrix representing the temperatures cube. The computation of the different voxels is shared at best between the available threads and blocks, according to the hardware.

For all methods, two matrices are used to model the cube and store the temperatures at times $t-1$ (previous state) and $t$ (current state) and swapped at each time step. In the multi-thread and GPU versions, it avoids concurrency clashes. The computation of voxels is illustrated on Fig.3.

As can be seen in Eq.12, the computation of the temperature at each voxel is depending on multiple parameters, such as time and space sampling, relaxation factor $\beta$, or the thermophysical properties detailed in Table 1. Some of them are constant over time and space, but other values have to be recomputed for each voxel. As we wanted this algorithm to be generic and compatible with other situations in the future (other types of thermal ablations, other types of experimental settings), we decided to pass all the constant data as arguments to the GPU kernel. This comes at the cost of time spent in memory transfer, but allows for a better flexibility. This reduces slightly the performance, as the gain in computation time is reduced by the time necessary for memory transfer. To improve speed, the constants could be programmed in the code directly, at the cost of flexibility. The heat capacity $C_{i,j,k}$ and the thermal conductivity $K_{i,j,k}$ at cell $i,j,k$ must be recomputed for each voxel, as they depend on the state of the corresponding cell, which itself depends on its previous temperature.

## 4 Results

### 4.1 Validation in-silico

Fig. 4 shows the results of the experiment with the gel parameters. Table 2 summarizes the maximum diameters of the ground truth isothermal surfaces at $0°$C, $-20°$C and $-40°$C (from [33]) and of the simulated iceballs, for the *IceRod* and the *IceEdge* cryoprobe models.

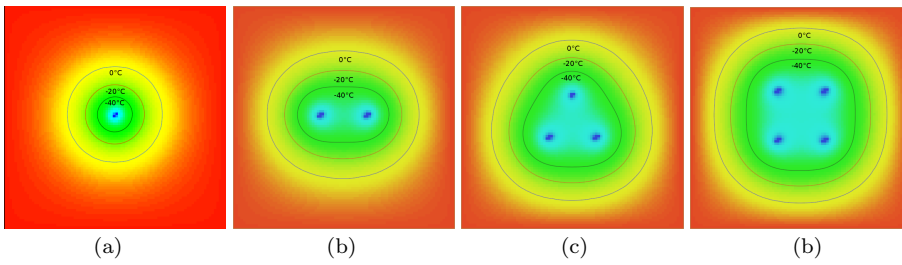(a)                    (b)                    (c)                    (b)

Fig. 4: Heat propagation simulation with different probes configurations, shown at end of the simulation (a-d). *IceEdge* parallel cryoprobes are evenly spaced 20mm apart (left to right). The figures show the largest 2D cross-sections of the iceball in the cryoprobe's axis. The color map is in the range $[-138.0, 37]°C$.

Table 2: Maximum diameters (mm) of ground truth and simulated iceball.

| Cryoprobe | # of needles | Ground truth [33] | | | Simulation | | |
|---|---|---|---|---|---|---|---|
| | | 0°C | -20°C | -40°C | 0°C | -20°C | -40°C |
| *IceEdge* | 1 | 43 | 33 | 24 | 40 | 29 | 21 |
| | 2 | 62 | 52 | 42 | 61 | 51 | 42 |
| | 3 | 69 | 59 | 49 | 64 | 53 | 44 |
| | 4 | 75 | 66 | 56 | 71 | 61 | 50 |
| *IceRod* | 1 | 36 | 26 | 18 | 39 | 27 | 18 |
| | 2 | 57 | 47 | 37 | 60 | 48 | 39 |
| | 3 | 62 | 52 | 44 | 61 | 50 | 40 |
| | 4 | 69 | 59 | 50 | 67 | 57 | 47 |

The results of the simulation are very close to the measurements, with a mean error of 0.28 mm, i.e. 5.8% of the diameter of the reference iceball. Note that the configuration of the multi-cryoprobe thermocouple matrix structure used in [33], which was designed with a minimum spacing of 5mm between the measuring thermocouples, which is a potential source of inaccuracy.

The simulation results were obtained with desktop PC equipped with a core-i7 3.40GHz CPU with 16Gb RAM and a GeForce GTX-1060 GPU with 6GB memory. The mean computation times of the simulation in CPU single thread and GPU implementations were of 540 secs. and 84 secs. respectively for a simulation in a $100×100×100$ mm$^3$ cube. The GPU implementation was on average $×6.4$ faster than the CPU implementation.

## 4.2 Validation on intraoperative MRI

The second experiment was conducted on a datasets of the five patient cases who underwent renal cryoablation. The cases have various characteristics in terms of the location of the tumor with respect to the blood vessel, the use of the dissection saline solution, and the number of cryoprobes as detailed in Table 3.

Simulations were performed for six different cube sizes: 60 mm, 70mm, 80 mm, 90mm, 100 mm, and 120mm, to evaluate the performance in terms of the computation time *vs.* results accuracy. The hardware used was the same as described in the in-silico experiment.
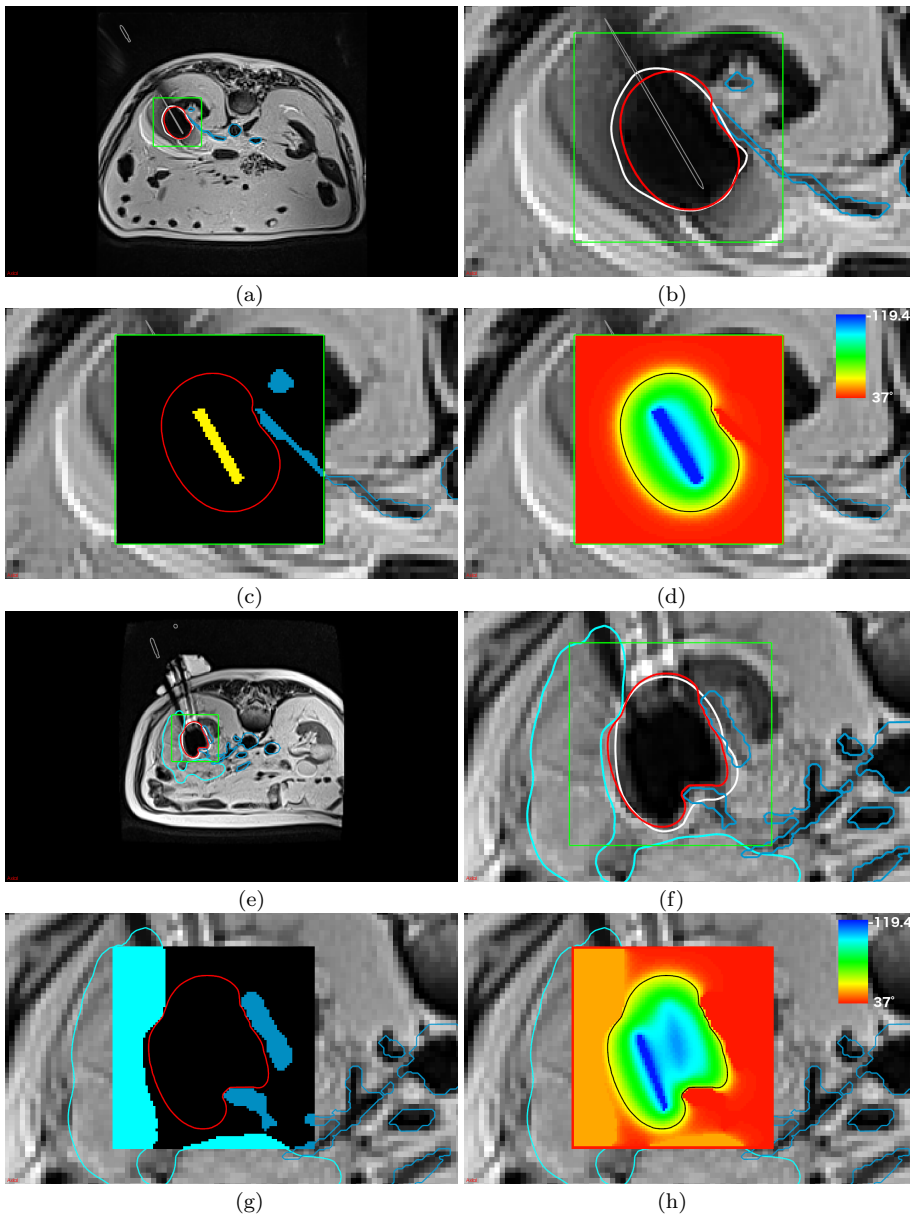
Fig. 5: Illustration of the simulation results at the end of the second freezing cycle of patient cases 2 (a-d) and 4 (e-h). In each group of 4 images, the top images (a,b and e,f respectively) show a representative intraoperative axial MRI slice (a and e full, b and f detail), with the 80 mm cube (green), the ground-truth iceball contour (white), the computed iceball contour (red), the blood vessels (dark blue) and the saline solution for case 4 (light blue). Images (c,g) show a detail of the same intraoperative axial MRI slice with the labels of the voxels inside the cube superimposed on them: freezing source (yellow), vessels and saline solution heating sources (blue) and iceball contour (red). Images (d,h) depict the temperature color map showing the $0°$C iso-surface (black); blue is the minimum freezing temperature of $-119.4°$C and red is the maximum body temperature of $37°$C. Note that the freezing sources are not visible on image (g) as the displayed slice does not intersects any of them, but image (h) shows the proximity of two of them.

Table 3: Characteristics of the patient cases.

| Patient case | Nearby vessels | Saline solution | Number of cryoprobes |
|:---:|:---:|:---:|:---:|
| 1 |  | yes | 4 |
| 2 | yes |  | 4 |
| 3 | yes |  | 3 |
| 4 | yes | yes | 4 |
| 5 |  |  | 5 |



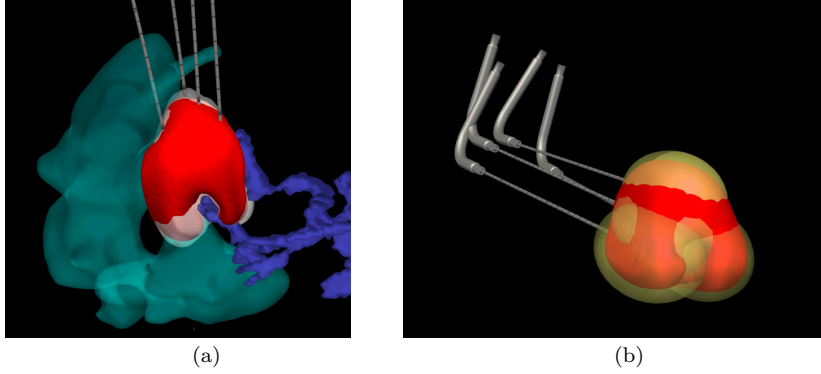(a)                                    (b)

Fig. 6: 3D views of: (a) ground truth (white) and simulated (red) iceballs, four cryoprobes (gray), blood vessels (dark blue) and saline solution (light blue); (b) simulated iceball (red) and theoretical ellipsoids (yellow) using measurements proposed in [33].

Fig. 5 and 6 show examples of the simulation results. Fig. 5 shows the simulated temperature distribution for cases 2 and 4 in a cube of 80 mm. Note how the presence of the blood vessels and the saline solution significantly influence the iceball shape.

Fig. 6a shows 3D views of the ground truth and simulated iceballs, the four cryoprobes, the blood vessels and the saline solution. Note that the simulated iceball is tightly fit around the blood vessels and is deformed by the saline solution. Fig. 6b shows the simulated iceball and the theoretical ellipsoidal iceball. Note the synergistic effect, the influence of the blood vessels and the saline solution that yield different iceball shape. This example illustrates the importance of a simulation based on an accurate simulation model rather than a theoretical one. The actual iceball differs significantly from theoretical ellipsoids and is smaller, which could lead to an insufficient ablation of the cancerous cells and a recurrence of the disease, or unexpected damages to surrounding structures.

Table 4 lists the Dice coefficients and the Hausdorff distances for the five patient cases and for the six cube sizes. These measurements indicate a close similarity between the two shapes, with an average Dice coefficient >0.79 in all cases.

However, this comparison is subjected to the possible errors in the manual segmentation which can introduce inaccuracies. The ground truth segmentation of the iceball in the MRI scans has an intrinsic uncertainty resulting from the scan resolution and structures contrast and the manual delineation process itself, which depend on subjective human factors [36]. As it is difficult to quantify this

Table 4: Dice coefficient and Hausdorff distance (HD, in mm.) measurements between the computed and the ground truth iceball segmentation shape at the end of the process (after the second freezing cycle), and computation times (in s.)

| Case | 60mm | | | 70mm | | | 80mm | | | 90mm | | | 100mm | | | 120mm | | |
|------|------|----|------|------|----|------|------|----|------|------|----|------|------|----|------|------|----|------|
| | Dice | HD | Time | Dice | HD | Time | Dice | HD | Time | Dice | HD | Time | Dice | HD | Time | Dice | HD | Time |
| 1 | 0.68 | 13.2 | 11.1 | 0.71 | 12.4 | 17.3 | 0.71 | 12.3 | 25.2 | 0.71 | 12.3 | 36.2 | 0.71 | 12.3 | 48.3 | 0.71 | 12.3 | 83.0 |
| 2 | 0.82 | 5.1 | 11.6 | 0.83 | 5.0 | 17.3 | 0.83 | 5.0 | 25.3 | 0.83 | 5.0 | 36.5 | 0.83 | 5.0 | 48.7 | 0.83 | 5.0 | 84.9 |
| 3 | 0.88 | 5.3 | 11.4 | 0.89 | 5.3 | 17.7 | 0.89 | 5.3 | 26.3 | 0.89 | 5.3 | 36.7 | 0.89 | 5.2 | 49.9 | 0.89 | 5.2 | 85.0 |
| 4 | 0.75 | 7.8 | 11.3 | 0.80 | 7.5 | 17.6 | 0.80 | 7.5 | 26.4 | 0.80 | 7.5 | 37.0 | 0.80 | 7.5 | 50.0 | 0.80 | 7.5 | 86.2 |
| 5 | 0.80 | 9.8 | 11.5 | 0.81 | 9.8 | 18.2 | 0.81 | 9.8 | 26.5 | 0.81 | 9.8 | 37.6 | 0.81 | 9.8 | 50.3 | 0.81 | 9.8 | 87.8 |
| Avg. | 0.79 | 8.20 | 11.4 | 0.81 | 8.0 | 17.6 | 0.81 | 8.0 | 26.0 | 0.81 | 8.0 | 36.8 | 0.81 | 8.0 | 49.4 | 0.81 | 8.0 | 85.4 |

uncertainty, the Dice coefficient and Hausdorff distance measures incorporate it in the comparison between the segmented and simulated iceball volumes.

We note that there is an additional phenomenon that reduces the accuracy of the simulated iceball. The interventions were all performed under MRI guidance using an MRI-compatible cryoprobe. The insulation of the cryoprobes is not sufficient to avoid a residual freezing along its body, resulting in an elongated shape along the cryoprobe, sometimes called by clinicians a "comet tail" (Fig. 7). When the freezing shaft is modeled as the only source of cold, without accounting for the residual cold along the body, the simulated iceball will not reproduce this comet tail, thereby leading to an inaccuracy of up to 10mm in the direction of the entry point. This explains why the Hausdorff distance may be >10mm.

A second source of inaccuracy is that the simulations where performed considering that all cryoprobes were used at full power during the intervention. However, there are situations in which the interventional radiologist reduces the power of one or several cryoprobes to protect a particular structure. This indeed occurred in patient case 5, as illustrated in Fig. 7b. In this case, the ground truth and the simulated iceball shapes will exhibit a looser match, as the simulation is less faithful. However, note that in this case the upper boundary of the ground truth and simulated iceball fit tightly.

In this study, we chose to fix the relaxation factor $\beta$ to 1.95. To test if this choice had influenced the results, we performed some additional experiments. With the 80mm cube, we computed the values of Dice and HD for each patient, using various values of $\beta$ chosen in the range $[1, 2]$. While there are differences in the results according to the values of $\beta$, these differences are not significant in 4 out of the 5 cases: $< 3\%$ Dice, $< 1.5$mm HD. For the case where there is a difference, the difference in Dice is 11% and the difference in HD is 2.2mm, which is most likely within the range of uncertainty and error of the many factors in the segmentation, model and simulation. Consequently, we conclude that the sensitivity to the value of beta is very moderate and that beta can be set to a fixed value.

In terms of computation times, the results in Table 4 indicate that the 80mm cube yields comparable accuracy than those of larger cubes with a significantly shorter computation time: 26.0 secs vs. $> 36.8$ secs on average. It seems enough to simulate an iceball with a reasonable accuracy even if the borders of the iceball seem close to the boundaries of the cube. The 70mm cube provides results quite comparable to the 80mm cube, and could be a reasonable alternative as well. The 60mm cube computes results twice faster, at the cost of a slightly lower accuracy. However, since the difference in accuracy is sub-millimetric, it is an option to be
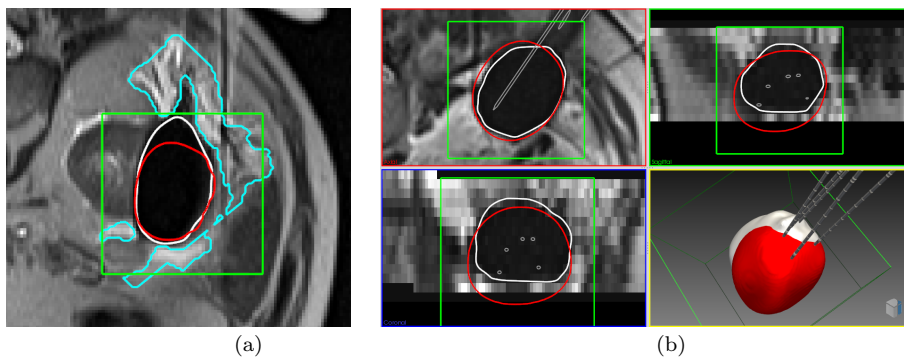
Fig. 7: (a) detail of an intraoperative axial MRI showing the "comet tail" effect in patient case 1. Superimposed are the cube (green), the ground-truth iceball contour (white), the computed iceball contour (red), and the saline solution (light blue); (b) detail of patient case 5 showing the two lower probes that were set to 60% of their freezing power. Both cases were computed within a 60mm cube.

Table 5: Computation times (in seconds) for the single thread, multi-thread, and GPU implementations for a $80 \times 80 \times 80\text{mm}^3$ cube.

| Patient case | Single thread | Multi-thread | GPU |
|---|---|---|---|
| 1 | 361.986 | 152.056 | 25.240 |
| 2 | 446.945 | 169.855 | 25.340 |
| 3 | 449.754 | 161.105 | 26.356 |
| 4 | 374.193 | 151.726 | 26.363 |
| 5 | 451.389 | 162.521 | 26.474 |
| Average | 416.853 | 159.453 | 25.955 |

considered to further reduce the computation time when needed. This of course depends on the number of cryoprobes used and the size of the resulting iceball that has to fit in such a small cube. In case of larger ablation volumes, larger cubes should be used.

Table 5 lists the computation times of the single-thread, multi-thread, and GPU variants of the algorithm, for the medium-sized cube of 80 mm. The results clearly show the advantage of the GPU computation. Note that the computation times do not depend on the complexity of the scene or on the number of heating structures. They only depend on the size of the cube and on the duration of the simulation process.

## 5 Conclusion

We have presented a new method for fast GPU-based iceball modeling based on the simulation of thermal propagation in the tissue based on the solution of the heat equation that accounts for the presence of heating sources around the iceball. Experimental results of two studies – an ex-vivo warm gel setup, and simulation on five retrospective patient cases of kidney tumors cryoablation with various levels of complexity of the vascular structure and warm saline solution around the

tumor tissue – indicate that our method yields accurate iceball shape predictions. The accurate results and short computation times indicate that our method can be effectively incorporated in a comprehensive cryoablation preoperative planning system that optimizes the number and location of cryoprobes and that takes into account the presence of blood vessels and warm saline solution.

Directions of future work include comprehensive experimental studies on larger datasets, more elaborate in-vivo and ex-vivo experimental results for ground truth. The simulation model can be extended to account for the comet tail effect and for the inclusion of cryoprobes with various properties, types, and power delivery characteristics.

**Compliance with ethical standards**

**Conflict of interest:** None of the authors has any conflict of interest. The authors have no personal financial or institutional interest in any of the materials, software or devices described in this article.

**Protection of human and animal rights statement:** No animals or humans were involved in this research. All images were anonymized before delivery to the researchers.

**Presentation at conferences:** This invited paper is a significantly expanded and detailed version of an paper presented at MICCAI 2018. The additions are a more detailed method section, a significantly extended state of the art, four new experimental cases, more cube sizes investigated, and an extended discussion.

# References

1. Gonder, M.J., Soanes, W.A., Smith, V.: Experimental prostate cryosurgery. Investigative urology **1** (1964) 610
2. Krunic, A.L., Marini, L.G.: Cryosurgery. In: European Handbook of Dermatological Treatments. Springer (2015) 1139–1149
3. Gage, A.A., Baust, J.: Mechanisms of tissue injury in cryosurgery. Cryobiology **37**(3) (1998) 171–186
4. Mazur, P.: Physical-chemical factors underlying cell injury in cryosurgical freezing. Technical report, Oak Ridge National Lab., Tenn. (1967)
5. Rezende, K.M., Moraes, P.d.C., Oliveira, L.B., Thomaz, L.A., Junqueira, J.L.C., Bönecker, M.: Cryosurgery as an effective alternative for treatment of oral lesions in children. Brazilian dental journal **25**(4) (2014) 352–356
6. Magalov, Z., Shitzer, A., Degani, D.: Isothermal volume contours generated in a freezing gel by embedded cryo-needles with applications to cryo-surgery. Cryobiology **55**(2) (2007) 127–137
7. Talbot, H., Lekkal, M., Béssard-Duparc, R., Cotin, S.: Interactive planning of cryotherapy using physically-based simulation. In: MMVR 21-Medicine Meets Virtual Reality-2014. (2014)
8. Hossain, S.C., Zhang, X., Haider, Z., Hu, P., Zhao, G.: Optimization of prostatic cryosurgery with multi-cryoprobe based on refrigerant flow. Journal of thermal biology **76** (2018) 58–67
9. Tsitskari, M., Georgiades, C.: Percutaneous cryoablation for renal cell carcinoma. Journal of kidney cancer and VHL **2**(3) (2015) 105–113

10. Young, J.L., McCormick, D.W., Kolla, S.B., Sountoulides, P.G., Kaufmann, O.G., Ortiz-Vanderdys, C.G., Huynh, V.B., Kaplan, A.G., Jain, N.S., Pick, D.L., Andrade, L.A., Os-ann, K.E., McDougall, E.M., Clayman, R.V.: Are multiple cryoprobes additive or synergistic in renal cryotherapy? Urology **79**(2) (2012) 484.e1 – 484.e6

11. Golkar, E., Rao, P.P., Joskowicz, L., Gangi, A., Essert, C.: Fast GPU Computation of 3D Isothermal Volumes in the Vicinity of Major Blood Vessels for Multiprobe Cryoablation Simulation. In: In proceedings of International Conference on Medical Image Computing and Computer-Assisted Intervention (MICCAI), Springer (2018) 230–237

12. Butz, T., Warfield, S.K., Tuncali, K., Silverman, S.G., van Sonnenberg, E., Jolesz, F.A., Kikinis, R.: Pre-and intra-operative planning and simulation of percutaneous tumor ablation. In: International Conference on Medical Image Computing and Computer-Assisted Intervention, Springer (2000) 317–326

13. Pennes, H.H.: Analysis of tissue and arterial blood temperatures in the resting human forearm. Journal of Applied Physiology **1**(2) (1948) 93–122

14. Deng, Z.S., Liu, J.: Numerical simulation of 3-D freezing and heating problems for combined cryosurgery and hyperthermia therapy. Numerical Heat Transfer, Part A: Applications **46**(6) (2004) 587–611

15. Ge, M., Chua, K., Shu, C., Yang, W.: Analytical and numerical study of tissue cryofreezing via the immersed boundary method. International Journal of Heat and Mass Transfer **83** (2015) 1–10

16. Ge, M., Shu, C., Chua, K., Yang, W.: Numerical analysis of a clinically-extracted vascular tissue during cryo-freezing using immersed boundary method. International Journal of Thermal Sciences **110** (2016) 109–118

17. Ge, M., Shu, C., Yang, W., Chua, K.: Incorporating an immersed boundary method to study thermal effects of vascular systems during tissue cryo-freezing. Journal of thermal biology **64** (2017) 92–99

18. Nabaei, M., Karimi, M.: Numerical investigation of the effect of vessel size and distance on the cryosurgery of an adjacent tumor. Journal of thermal biology **77** (2018) 45–54

19. Zhang, X., Hossain, S.C., Zhao, G., Qiu, B., He, X.: Two-phase heat transfer model for multiprobe cryosurgery. Applied Thermal Engineering **113** (2017) 47 – 57

20. Kumar, A., Kumar, S., Katiyar, V., Telles, S.: Phase change heat transfer during cryosurgery of lung cancer using hyperbolic heat conduction model. Computers in Biology and Medicine **84** (2017) 20 – 29

21. Kumar, M., Upadhyay, S., Rai, K.: A study of cryosurgery of lung cancer using modified legendre wavelet galerkin method. Journal of Thermal Biology **78** (2018) 356 – 366

22. Keelan, R., Zhang, H., Shimada, K., Rabin, Y.: Graphics processing unit-based bioheat simulation to facilitate rapid decision making associated with cryosurgery training. Technology in cancer research & treatment **15**(2) (2016) 377–386

23. Villard, C., Soler, L., Papier, N., Agnus, V., Thery, S., Gangi, A., Mutter, D., Marescaux, J.: Virtual radiofrequency ablation of liver tumors. In: Surgery Simulation and Soft Tissue Modeling. Springer (2003) 366–374

24. Villard, C., Soler, L., Gangi, A.: Radiofrequency ablation of hepatic tumors: simulation, planning, and contribution of virtual reality and haptics. Computer Methods in Biomechanics and Biomedical Engineering **8**(4) (2005) 215–227

25. Huang, H.W.: Influence of blood vessel on the thermal lesion formation during radiofrequency ablation for liver tumors. Medical Physics **40**(7) (2013) 073303

26. Dos Santos, I., Haemmerich, D., Schutt, D., da Rocha, A.F., Menezes, L.R.: Probabilistic finite element analysis of radiofrequency liver ablation using the unscented transform. Physics in Medicine & Biology **54**(3) (2009) 627

27. Shao, Y., Arjun, B., Leo, H., Chua, K.: A computational theoretical model for radiofrequency ablation of tumor with complex vascularization. Computers in biology and medicine **89** (2017) 282–292

28. Rieder, C., Kroeger, T., Schumann, C., Hahn, H.K.: GPU-based Real-Time Approximation of the Ablation Zone for Radiofrequency Ablation. IEEE Transactions on Visualization and Computer Graphics **17**(12) (2011) 1812–1821

29. Mariappan, P., Weir, P., Flanagan, R., Voglreiter, P., Alhonnoro, T., Pollari, M., Moche, M., Busse, H., Futterer, J., Portugaller, H.R., Blanco Sequeiros, R., Kolesnik, M.: GPU-based RFA simulation for minimally invasive cancer treatment of liver tumours. International journal of computer assisted radiology and surgery **12**(1) (2017) 59–68

30. Audigier, C., Mansi, T., Delingette, H., Rapaka, S., Mihalef, V., Carnegie, D., Boctor, E., Choti, M., Kamen, A., Ayache, N., Comaniciu, D.: Efficient lattice boltzmann solver for

patient-specific radiofrequency ablation of hepatic tumors. IEEE Transactions on Medical Imaging **34**(7) (2015) 1576–1589

31. Patil, H.M., Maniyeri, R.: Finite difference method based analysis of bio-heat transfer in human breast cyst. Thermal Science and Engineering Progress **10** (2019) 42–47

32. Blomberg, T.: Heat conduction in two and three dimensions: Computer modelling of building physics applications. PhD thesis, Department of Building Physics, Lund University, Sweden (1996) Report TVBH1008, ISBN 91-88722-05-8.

33. Shah, T.T., Arbel, U., Foss, S., Zachman, A., Rodney, S., Ahmed, H.U., Arya, M.: Modeling cryotherapy ice ball dimensions and isotherms in a novel gel-based model to determine optimal cryo-needle configurations and settings for potential use in clinical practice. Urology **91** (2016) 234–240

34. Choi, J., Bischof, J.C.: Review of biomaterial thermal property measurements in the cryogenic regime and their use for prediction of equilibrium and non-equilibrium freezing applications in cryobiology. Cryobiology **60**(1) (2010) 52–70

35. Nolden, M., Zelzer, S., Seitel, A., Wald, D., Müller, M., Franz, A.M., Maleike, D., Fangerau, M., Baumhauer, M., Maier-Hein, L., Maier-Hein, K.H., Meinzer, H.P., Wolf, I.: The medical imaging interaction toolkit: challenges and advances. International journal of computer assisted radiology and surgery **8**(4) (2013) 607–620

36. Joskowicz, L., Cohen, D., Caplan, N., Sosna, J.: Inter-observer variability of manual contour delineation of structures in ct. European radiology **29**(3) (2019) 1391–1399